Lawrence Berkeley National Laboratory

Lawrence Berkeley National Laboratory

Title

Image properties of list mode likelihood reconstruction for a rectangular positron emission mammography with DOI measurements

Permalink

https://escholarship.org/uc/item/08j9w45w

Authors

Qi, Jinyi
Klein, Gregory J.
Huesman, Ronald H.

Publication Date

2000-10-01

eScholarship.org Powered by the California Digital Library
University of California

Image Properties of List Mode Likelihood Reconstruction for a Rectangular Positron Emission Mammograph with DOI Measurements

Jinyi Qi, *Member, IEEE*, Gregory J. Klein, *Member, IEEE*, and Ronald H. Huesman, *Senior Member, IEEE*

Abstract—**A positron emission mammography scanner is under development at our Laboratory. The tomograph has a rectangular geometry consisting of four banks of detector modules. For each detector, the system can measure the depth of interaction information inside the crystal. The rectangular geometry leads to irregular radial and angular sampling and spatially variant sensitivity that are different from conventional PET systems. We adapted the theoretical analysis that we had developed for conventional PET systems to the list mode likelihood reconstruction for this tomograph. The local impulse response and covariance of the reconstruction can be easily computed using FFT. These theoretical results are also used with computer observer models to compute the signal-to-noise ratio for lesion detection. The analysis reveals the spatially variant resolution and noise properties of the list mode likelihood reconstruction. The theoretical predictions are in good agreement with Monte Carlo results.**

I. Introduction

A rectangular positron emission tomograph (Fig. 1), dedicated to imaging the human breast, is under development at our Laboratory [1]. The tomograph consists of four banks of detector modules (two banks of 3×3 modules left and right and two banks of 3×4 modules top and bottom). Each module consists of an 8×8 array of 3mm×3mm×30mm lutetium oxyorthosilicate (LSO) crystals. The maximum field of view (FOV) of the system is 96×72×72 mm^3. Each detector module is coupled to a 8×8 photodiode array at the front and a photo multiplier tube (PMT) at the end [2]. Using the ratio between the signal from the photodiode and the PMT, the system measures the depth of interaction (DOI) of the photon inside each crystal and encodes it with three bits. Each detector is placed in coincidence with all detectors in the other three banks, giving rise to 172 million possible lines of response (LORs).

The data from the new tomograph is stored in list mode format because the total number of detections will generally be far less than the total number of LORs. We have developed a list mode likelihood reconstruction algorithm for the tomograph [3]. The DOI information was explicitly modeled in the forward projection for each LOR. The rectangular geometry leads to irregular radial and angular sampling and spatially variant sensitivity that are very different from conventional PET systems. Therefore, it is of importance to study the image properties of the reconstructions. We adapted the theoretical analysis that we had developed for conventional PET systems [4], [5] to the list mode likelihood reconstruction for this tomograph. The local impulse response and covariance of the reconstruction can be easily computed using FFT techniques. These results can then be used with computer observer models to compute the signal-to-noise ratio (SNR) for lesion detection.

This work was supported by the U.S. Department of Health and Human Services under grant P01 HL25840 and by the Director, Office of Science, Office of Biological and Environmental Research, Medical Sciences Division of the US Department of Energy under contract DE-AC03-76SF00098.

J. Qi, G. J. Klein, and R. H. Huesman are with the Center for Functional Imaging, Lawrence Berkeley National Laboratory, Berkeley, CA 94720 USA (telephone: 510-486-4695, e-mail: jqi@lbl.gov).

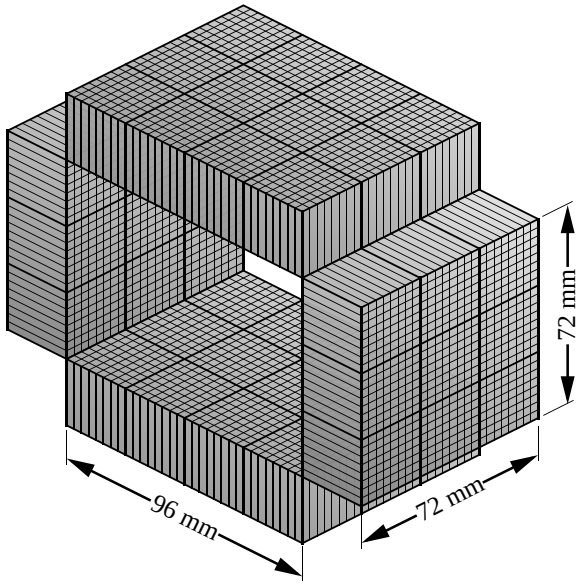

Fig. 1. PEM Geometry.

II. Theory

A. List Mode Likelihood Reconstruction

Histogrammed PET data are generally modeled as a collection of independent Poisson random variables. By treating the detections in each LOR separately, we can derive the appropriate log-likelihood function for list mode data [3]:

$$L(\boldsymbol{x}) = \sum_{k=1}^{K} \log \sum_{j=1}^{N} p(i_k, j) x_j - \sum_{j=1}^{N} \varepsilon_j x_j, \qquad (1)$$

where x_j is the mean activity inside the j^{th} voxel of the unknown image, $p(i,j)$ is the probability of detecting an event from the j^{th} voxel in the i^{th} LOR, i_k is the index of the LOR of the k^{th} detection, $\varepsilon_j \equiv \sum_i p(i,j)$, K is the total number of detections, and N is the total number of image voxels. Randoms and scatters are ignored in this model.

The maximum likelihood (ML) estimate can be found by maximizing (1). A popular ML algorithm for PET reconstruc-

tion is the expectation maximization (EM) algorithm [6], [7], [8]. However, the ML solution is unstable (i.e. noisy), because the tomography problem is ill-conditioned. Hence some form of regularization (or prior function) is needed to reconstruct a reasonable image. The prior function used in [3] is a Gaussian prior whose logarithm is of the form

$$\beta U(\boldsymbol{x}) = \frac{\beta}{2}(\boldsymbol{x}-\boldsymbol{m})'\boldsymbol{R}(\boldsymbol{x}-\boldsymbol{m}), \tag{2}$$

where β is the smoothing parameter, $\boldsymbol{m}$ is the estimated mean of the unknown image, $\boldsymbol{R}$ is a positive definite (or semidefinite) matrix.

Combining the likelihood function (1) and the image prior (2), the reconstruction is found as:

$$\hat{\boldsymbol{x}} = \arg\max_{\boldsymbol{x}\geq 0} \left[L(\boldsymbol{x}) - \beta U(\boldsymbol{x})\right]. \tag{3}$$

For further simplification, $\boldsymbol{R}$ is chosen to be a diagonal matrix, so the EM algorithm can be used to solve (3). The EM update equation is [3]

$$\hat{x}_j^{n+1} = \frac{1}{2}\left(m_j - \frac{\varepsilon_j}{\beta r_{jj}}\right) + \sqrt{\frac{1}{4}\left(m_j - \frac{\varepsilon_j}{\beta r_{jj}}\right)^2 + \frac{\hat{x}_j^n}{\beta r_{jj}} \sum_{k=1}^{K} \frac{p(i_k, j)}{\sum_{l=1}^{N} p(i_k, l)\hat{x}_l^n}},$$

where r_{jj} is the (j,j)th element of $\boldsymbol{R}$.

B. Approximation of Local Impulse Response and Covariance

Since the estimator (3) is non-linear, its image properties are object dependent. Therefore, we study the image properties locally for each voxel using the local impulse response and covariance. The local impulse response of the jth voxel is defined as

$$\boldsymbol{l}^j(\hat{\boldsymbol{x}}) = \lim_{\delta\to 0} \frac{\mathcal{E}\hat{\boldsymbol{x}}[\boldsymbol{x}+\delta\boldsymbol{e_j}] - \mathcal{E}\hat{\boldsymbol{x}}[\boldsymbol{x}]}{\delta} \tag{4}$$

where $\hat{\boldsymbol{x}}[\boldsymbol{x}]$ denotes the reconstruction of a random data set generated by the source distribution $\boldsymbol{x}$, $\mathcal{E}$ denotes expectation and $\boldsymbol{e_j}$ is the jth unit vector. One scalar measure of resolution is the local contrast recovery coefficient (CRC) defined as the peak value of the local impulse response, i.e., $\mathrm{crc}_j \equiv l_j^j(\hat{\boldsymbol{x}})$.

Using the results derived in [5] and noting that matrix $\boldsymbol{R}$ is diagonal, we can approximate $l^j(\hat{\boldsymbol{x}})$ in the following compact form

$$l^j(\hat{\boldsymbol{x}}) \approx \boldsymbol{Q}'\mathrm{diag}\left[\frac{\lambda_i(j)}{\lambda_i(j)+\beta r_{jj}}\right]\boldsymbol{Q}\boldsymbol{e_j} \tag{5}$$

where $\{\lambda_i(j),\quad i = 1,\ldots,N\}$ is the Fourier transform of the local invariant approximation[1] of the j^{th} column of the Fisher information matrix defined as $\boldsymbol{F} \equiv \boldsymbol{P}'\mathrm{diag}\left[\sum_{j=1}^{N} p(i,j)x_j\right]^{-1}\boldsymbol{P}$, $\boldsymbol{Q}$ and $\boldsymbol{Q}'$ represent the Kronecker form of the FFT and its inverse, respectively. The $\boldsymbol{P}$ is the detection probability matrix with the $(i,j)^{th}$ element being $p(i,j)$. Then the crc_j is

$$\mathrm{crc}_j \approx \frac{1}{N}\sum_{i=1}^{N}\left[\frac{\lambda_i(j)}{\lambda_i(j)+\beta r_{jj}}\right]. \tag{6}$$

Similarly, the covariance at voxel j can be approximated by

$$\mathrm{Cov}_j(\hat{\boldsymbol{x}}) \approx \boldsymbol{Q}'\mathrm{diag}\left[\frac{\lambda_i(j)}{(\lambda_i(j)+\beta r_{jj})^2}\right]\boldsymbol{Q}\boldsymbol{e_j}, \tag{7}$$

and the variance at voxel j as

$$\mathrm{var}_j \approx \frac{1}{N}\sum_{i=1}^{N}\left[\frac{\lambda_i(j)}{(\lambda_i(j)+\beta r_{jj})^2}\right]. \tag{8}$$

Interested readers are referred to [5] for details in the derivation. The major approximations used are the first order Taylor series expansion and the locally shift invariant approximation. Thus (5)-(8) work the best when the log-posterior density function is locally quadratic and $l^j(\hat{\boldsymbol{x}})$ has compact support and is shift invariant within its support.

A Note on FWHM

For a linear algorithm, resolution is characterized by measuring the full-width-at-half-maximum (FWHM) of the point spread function. Generally the noise level is correlated to the FWHM: the larger the FWHM, the less the noise. However, this is not strictly true for statistical reconstruction. An example is the regularized ML reconstruction we use here. Considering (5), when β is very large ($\gg \lambda_i(j)/r_{jj}$), we get

$$l^j(\hat{\boldsymbol{x}}) \approx \frac{1}{\beta r_{jj}}\boldsymbol{Q}'\mathrm{diag}\left[\lambda_i(j)\right]\boldsymbol{Q}\boldsymbol{e_j} \tag{9}$$

As β increases, the amplitude of $l^j(\hat{\boldsymbol{x}})$ decreases, and so does the noise level (see (7)), but the FWHM of $l^j(\hat{\boldsymbol{x}})$ remains the same because the shape of $l^j(\hat{\boldsymbol{x}})$ is determined by $\boldsymbol{Q}'\mathrm{diag}\left[\lambda_i(j)\right]\boldsymbol{Q}\boldsymbol{e_j}$ and is independent of β. In this case, even though the MAP reconstruction is pulled towards the prior mean, the significant elements of $l^j(\hat{\boldsymbol{x}})$ always have a finite (and relatively small) support. Hence (5)-(8) still hold for large β here.

C. SNR of Lesion Detection

Combining these results with computer observer models [10], we can derive approximate theoretical expression for SNR of detecting a cancerous lesion in the reconstructed images [9]. For each reconstruction $\hat{\boldsymbol{x}}$, a computer observer computes a test statistic $\eta(\hat{\boldsymbol{x}})$ based on some numerical model and compares the statistic to a decision threshold: if $\eta(\hat{\boldsymbol{x}})$ exceeds the threshold, $\hat{\boldsymbol{x}}$ is determined to have a lesion; otherwise, it is not. The lesion detectability can be measured by the SNR of the computer observer that is defined as

$$\mathrm{SNR}^2 = \frac{(\bar{\eta}_1 - \bar{\eta}_0)^2}{\mathrm{var}[\eta]}, \tag{10}$$

where $\bar{\eta}_1$ and $\bar{\eta}_0$ are the ensemble means of the test statistics of the reconstructions with and without lesion present, respectively.

[1] $\boldsymbol{\lambda}(j)$ is computed as follows: (1) compute the image of $\boldsymbol{P}'\mathrm{diag}\left[\sum_{j=1}^{N} p(i,j)x_j\right]^{-1}\boldsymbol{P}\boldsymbol{e_j}$ and shift the maximum value to the image center; (2) make the image symmetry so that its Fourier transform coefficients are real; (3) take the Fourier transform and set any negative value to zero.

One simple observer model is to use the maximum contrast at the lesion location as the test statistic. For a unit voxel lesion (the lesion that is equal to the unit vector), the SNR of this contrast observer is just the contrast-to-noise ratio (CNR) defined as [4]

$$\mathrm{CNR} \equiv \frac{crc_j}{\sqrt{var_j}}. \tag{11}$$

The contrast observer is generally considered as "too simple", but we will show later that it achieves the maximum SNR in lesion detection here.

Another popular observer model is the non-prewhitening (NPW) observer, which computes the following test statistic [10]

$$\eta_{\mathrm{NPW}}(\hat{\boldsymbol{x}}) = \left(\mathcal{E}\hat{\boldsymbol{x}}[\boldsymbol{x}+\boldsymbol{e_j}] - \mathcal{E}\hat{\boldsymbol{x}}[\boldsymbol{x}]\right)' \hat{\boldsymbol{x}}, \tag{12}$$

where $\boldsymbol{x}$ denotes the background and $\boldsymbol{e_j}$ the unit voxel lesion.

The SNR of the NPW observer is

$$\begin{aligned}\mathrm{SNR}^2_{\mathrm{NPW}} &= \frac{\left[\left(\mathcal{E}\hat{\boldsymbol{x}}[\boldsymbol{x}+\boldsymbol{e_j}] - \mathcal{E}\hat{\boldsymbol{x}}[\boldsymbol{x}]\right)' \left(\mathcal{E}\hat{\boldsymbol{x}}[\boldsymbol{x}+\boldsymbol{e_j}] - \mathcal{E}\hat{\boldsymbol{x}}[\boldsymbol{x}]\right)\right]^2}{\mathrm{var}[\eta_{\mathrm{NPW}}(\hat{\boldsymbol{x}})]} \\ &\approx \frac{\left\{[l^j(\hat{\boldsymbol{x}})]'[l^j(\hat{\boldsymbol{x}})]\right\}^2}{[l^j(\hat{\boldsymbol{x}})]'\boldsymbol{\Sigma}[l^j(\hat{\boldsymbol{x}})]}\end{aligned} \tag{13}$$

where $\boldsymbol{\Sigma}$ is the covariance matrix of $\hat{\boldsymbol{x}}$. Here we assume that the lesion is so small that its presence does not change the covariance of the reconstruction.

By assuming that the covariance around voxel j is locally stationary, $\boldsymbol{\Sigma}$ in (13) can be approximated by

$$\boldsymbol{\Sigma} \approx \boldsymbol{Q}'\mathrm{diag}\left[\frac{\lambda_i(j)}{(\lambda_i(j)+\beta r_{jj})^2}\right]\boldsymbol{Q}. \tag{14}$$

Note the above approximation is dependent on the location of the lesion.

Substituting (5) and (14) into (13), we get [9]

$$\begin{aligned}\mathrm{SNR}^2_{\mathrm{NPW}} &\approx \left(\sum_{i=1}^{N}\left(\frac{\lambda_i(j)}{\lambda_i(j)+\beta r_{jj}}\right)^2\right)^2 \\ &\quad \times \left(N\sum_{i=1}^{N}\frac{\lambda_i^3(j)}{(\lambda_i(j)+\beta r_{jj})^4}\right)^{-1}.\end{aligned} \tag{15}$$

In Fig. 2 we plot the performance of the two computer observers as a function of smoothing parameter with $r_{jj} = 1$. Each curve corresponds to a point of interest selected in Section III.B. The $p(i,j)$'s for each LOR were computed as described in [3] with 729 line integrals and including self-attenuation and crystal penetration effects. The $\lambda_i(j)$'s are normalized so that $\sum_{i=1}^{N}\lambda_i(j) = N$ for all j. Therefore, the maximum SNR of any linear observer (achievable with the prewhitening observer) is 1. This maximum value will be increased by the increase in count level and lesion contrast in real situations. The plots show that the CNR monotonically increases as β increases and reaches the maximum (1.0) when β is very large; on the other hand, the $\mathrm{SNR}_{\mathrm{NPW}}$ reaches its maximum value (around 0.9) when $\beta \approx 2.0$. The contrast observer outperforms the NPW observer in detecting a unit voxel lesion. Moreover, the contrast observer achieves the best performance in detection that is generally only achievable with the prewhitening observer. The monotonic increase of the CNR is somewhat counterintuitive. Note, however, these plots are only valid for the prior used here (diagonal matrix $\boldsymbol{R}$). For other priors, the monotonic increase CNR may not exist (see Fig. 3 in [4] for examples of CNR for pair-wise difference priors). This may indicate the contrast observer is perfectly suitable for detecting lesions in a uniform background. We plan to verify this with receiver operating characteristics (ROC) studies.

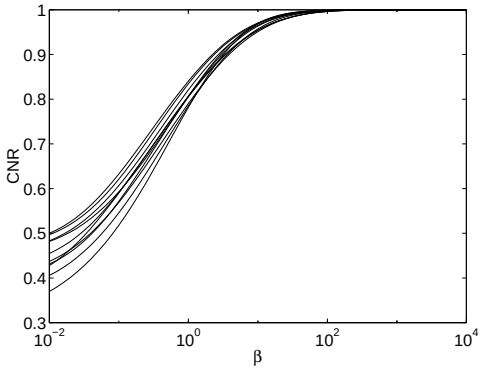

(a)

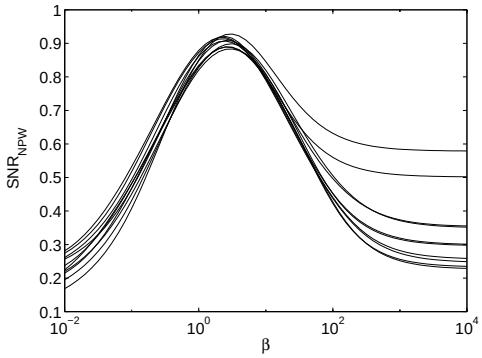

(b)

Fig. 2. (a) Plots of CNR as a function of β for the ten selected points of interest. (b) Plots of $\mathrm{SNR}_{\mathrm{NPW}}$ as a function of β for the ten selected points of interest.

III. Simulations

For breast imaging with F-18-labeled deoxyglucose (FDG), we can assume that the FOV is filled with uniform activity and that features such as cancerous lesions account for a small fraction of the radioactivity. Therefore, we used a uniform flood source as background. For simulations of acquired data, a linear attenuation coefficient of 0.01 mm^{-1} was used for self-attenuation, and a linear attenuation coefficient of 0.1 mm^{-1} was used for crystal penetration. The total number of detections from the background was about 2.3 million, calculated by assuming a 1 minute scan of a subject weighting 70 kg, and an injection of 1 mCi of FDG which was uniformly distributed inside the body. List mode data were generated by tracing the two back-to-back photons generated by each positron annihilation. Photons that interact in any way in the field of view are assumed undetected, and photons that interact in the detectors are assumed to do so once in a single well-defined depth decoded portion of a scintillator crystal. The images were recon-

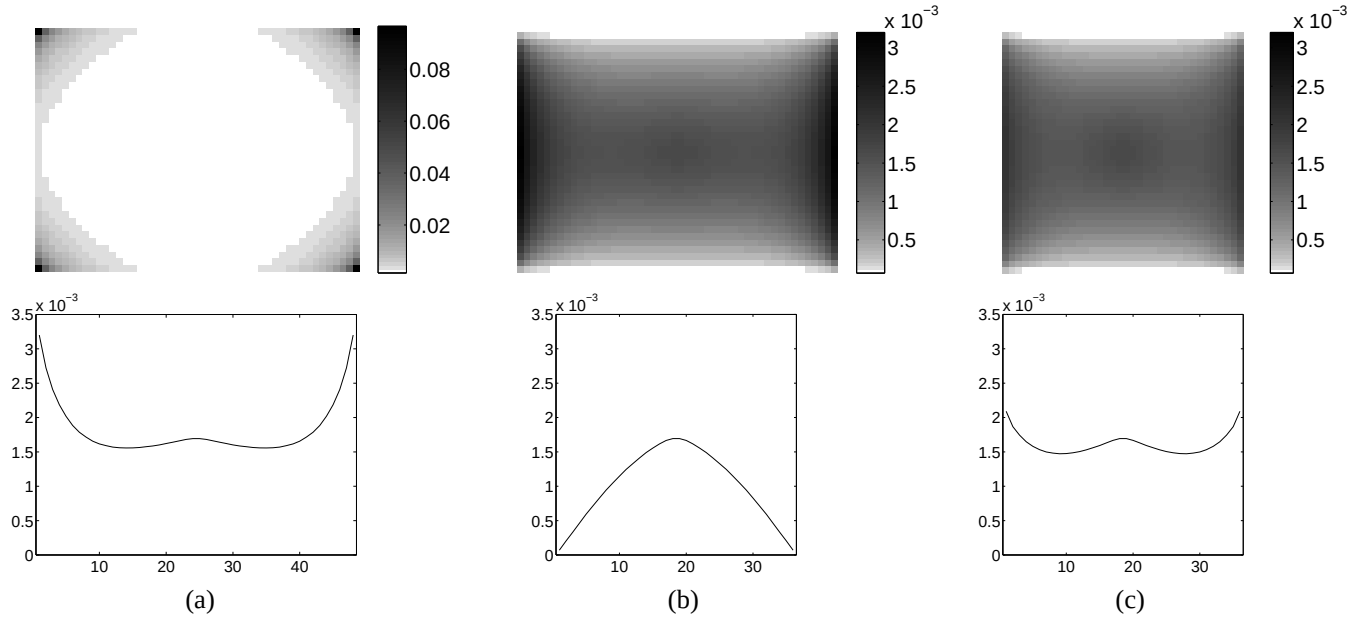

Fig. 3. The transaxial view and its center horizontal profile (a), coronal view and its center vertical profile (b), and sagittal view and its center horizontal profile (c) of the sensitivity image through the voxel of (25,19,19). Note each view is individually scaled.

structed with 48×36×36 2mm cube voxels using the algorithm described in [3]. The $p(i,j)$'s for each event were computed using 729 line integrals. The algorithm was run until convergence, which was defined when the absolute value of the relative change of each voxel became less than 0.0001.

A. Spatially Variant Sensitivity

We study the spatially variant sensitivity of the rectangular tomograph by computing the diagonal elements of the Fisher information matrix for a uniform background

$$f_{jj} = \sum_i \frac{p(i,j)^2}{\sum_k p(i,k) x_k}, \tag{16}$$

where $\sum_i$ is the sum over all possible LORs and $x_k = 1$. Note $f_{jj} = \sum_{i=1}^{N} \lambda_i(j)/N$. It partly controls the resolution and noise trade off as shown in (5)-(8), and is different from the photon detection sensitivity ε_j in (1).

The result is shown in Fig. 3. Clearly, the four corners in the transaxial view have the highest sensitivity because the detectors are closer to each other and hence the projection lines that intersect them pass through very few other voxels. The next level of sensitivity is the set of voxels near the detector face because of a similar reason. The top and the bottom axial planes have the least sensitivity.

The highly variant sensitivity determines the spatially variant resolution and noise properties in reconstructions. If we can assume that the $\{\lambda_i(j), i = 1, \ldots, N\}$ for all the voxels have the same shape and the only difference between them is their mean value, i.e.

$$\lambda_i(j) = f_{jj} \bar{\lambda}_i, \tag{17}$$

where $\bar{\lambda}_i$ is the normalized frequency response with $\sum_{i=1}^{N} \bar{\lambda}_i = N$, then (6) and (8) can be changed to

$$\mathrm{crc}_j \approx \frac{1}{N} \sum_{i=1}^{N} \left[\frac{\bar{\lambda}_i}{\bar{\lambda}_i + \beta r_{jj}/f_{jj}} \right]. \tag{18}$$

$$\mathrm{var}_j \approx \frac{1}{N f_{jj}} \sum_{i=1}^{N} \left[\frac{\bar{\lambda}_i}{(\bar{\lambda}_i + \beta r_{jj}/f_{jj})^2} \right]. \tag{19}$$

It shows that the CRC at voxel j is controlled by $\beta r_{jj}/f_{jj}$, and the variance is controlled by both $\beta r_{jj}/f_{jj}$ and f_{jj} itself. Both of them are spatially variant if βr_{jj} is constant for all j's. If, however, we choose $r_{jj} = f_{jj}$, then CRC is constant for all voxels, and the variance is inversely proportional to the sensitivities f_{jj}. This property is desirable because the spatial variation of CRC is removed, and the variation of variance is easier to predict as well. Therefore, we use this weighting scheme ($r_{jj} = f_{jj}$) in the following reconstructions. Although the assumption (17) does not strictly hold in real situations, it is a reasonable approximation as shown in the following simulation results.

B. Local Impulse Response

We selected ten points of interest in the FOV, five in the center axial plane and five in an off-center axial plane, for studying local impulse response functions. We chose the smoothing parameter $\beta = 50$. First, the local impulse responses were measured by computing the difference between the reconstruction of the background plus a point source and the reconstruction of the sole background. In this study, we only used one list mode data set for the uniform background (2 million events) and did not average over an ensemble of reconstructions. However, the point sources were chosen to have relative high count (10:1 ratio) so that the noise in the measured local impulse response function should be small. Fig. 4 shows the surface plots of the measured local impulse response functions. Each plot was a summation of 5 individually computed local impulse response functions in

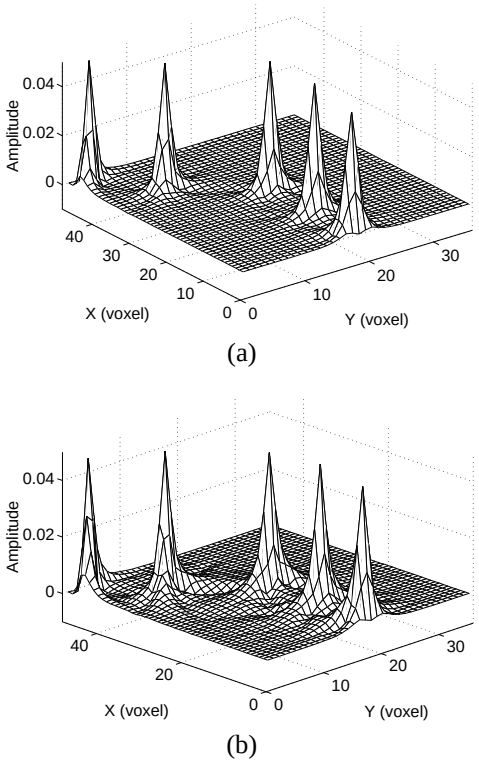

Fig. 4. Surface plots of the measured local impulse response functions. (a) Five points of interest in the axial center plane; (b) five points of interest in the third plane from the axial boundary.

the same axial plane. Despite the spatially variant sensitivity, the local impulse responses shown in Fig. 4 have nearly constant CRCs. This shows the effectiveness of the weighting of $r_{jj} = f_{jj}$. If $r_{jj} = 1$, the effective smoothing parameter for each point would be β / f_{jj} as shown in (18). Hence the CRC would be spatially variant as a function of f_{jj}: the center plane would have higher CRCs than the axial boundary plane, and within each plane, the corner voxel would have higher CRC than other locations.

Second, we compute the local impulse response functions using (5). Fig. 5 shows the comparison of the contour plots of the measured local impulse response functions and the theoretical approximations using (5) for the five points in the axial center plane. It shows that the theoretical approximations closely match the measurements. The different shape of the local impulse response for different point shows that the assumption in (17) does not strictly hold. In addition, if the background is not uniform, more mismatch could be expected for locations near the structural boundaries because their local impulse response functions would have more irregular shapes.

C. Variance

We computed the voxel-wise variance image using 200 independent Monte Carlo reconstructions and compared with the theoretical prediction from (8). The smoothing parameter β was 50. Fig. 6 shows the transaxial, coronal and sagittal views of the relative standard deviation images through the center voxel in the FOV. Fig. 7 shows the comparison of two profiles through the relative standard deviation images. Strictly speaking, to

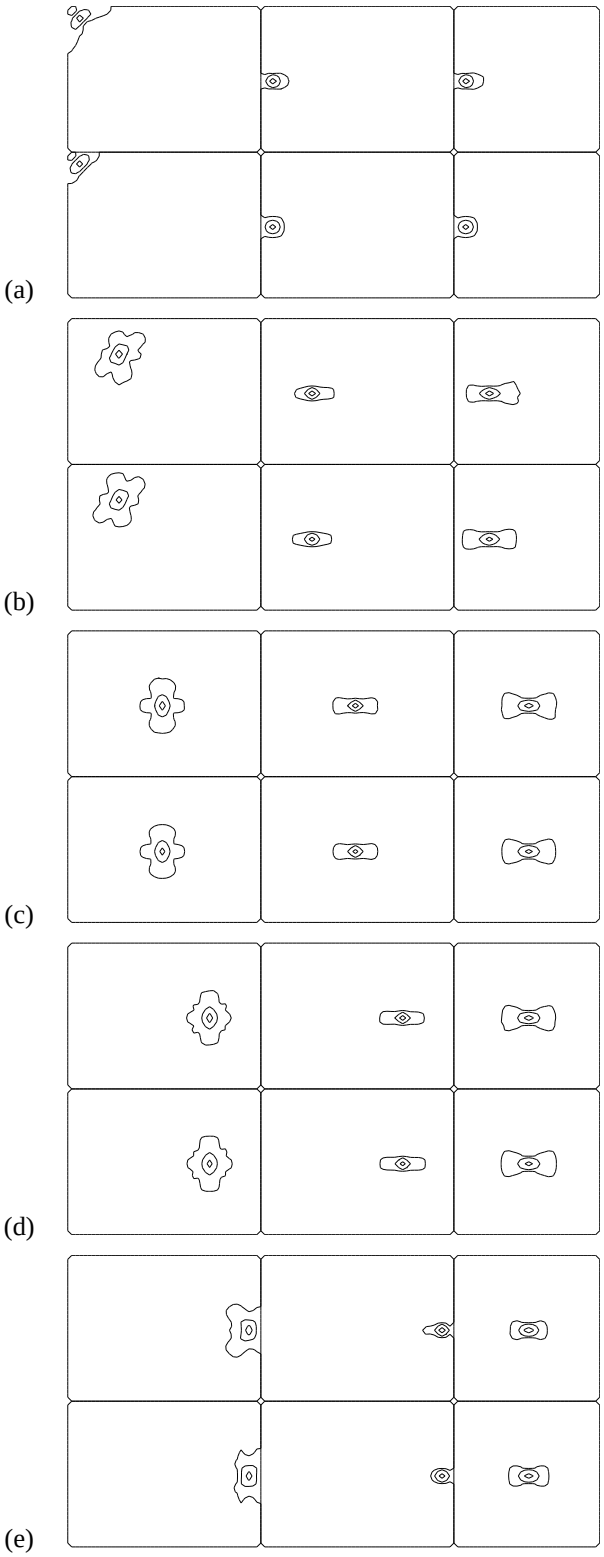

Fig. 5. The transaxial (left column), coronal (center column), and sagittal (right column) contour plots of the measured local impulse response (top row) and the theoretical approximations (bottom row) for the 5 points of interest in the axial center plane: (a) point (2,2,18); (b) point (12,8,18); (c) point (24,18,18); (d) point (36,18,18); (e) point (46,18,18). The contours correspond to, from inside to outside, .5, 0.1, 0.01 of the maximum of each response, respectively.

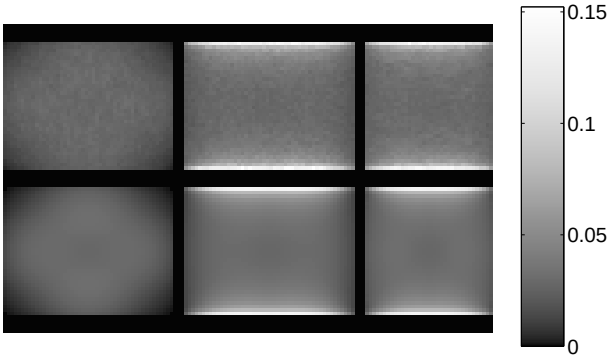

Fig. 6. Comparison of the relative standard deviation images from Monte Carlo reconstructions (top row) and theoretical predication (bottom row). From left to right, the images are transaxial, coronal, and sagittal views of the standard deviation images through the center voxel.

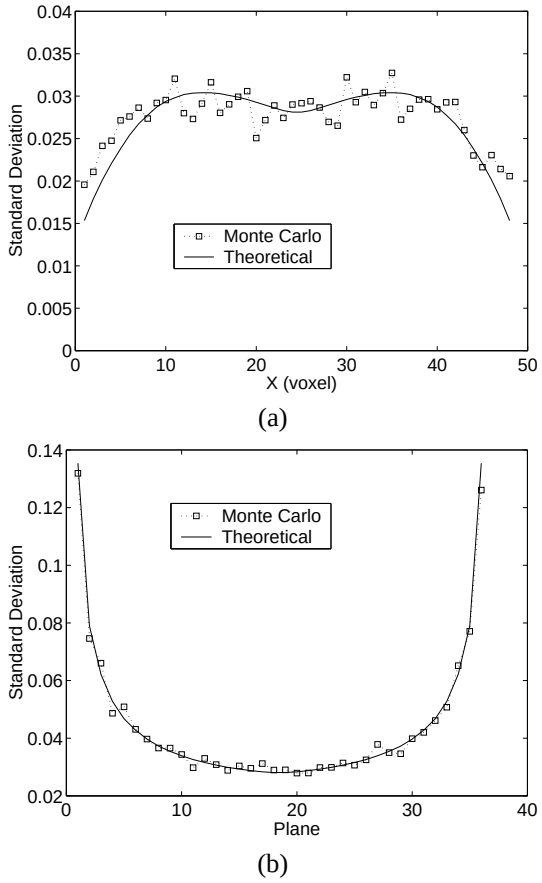

Fig. 7. Comparison of the relative standard deviation profiles: (a) horizontal profiles through the center of the transaxial view in Fig. 6; (b) vertical profiles through the center of the sagittal view in Fig. 6.

compute the variance image using (8) requires the computation of $\lambda_i(j)$ for all the voxels. This would require a large amount of computing time. Here we used the $\lambda_i(j)$ of the center voxel in each axial plane for all the voxels inside that plane. This approximation caused under-estimation of the variance around the corner regions as shown in the transaxial view in Fig. 6. In general, the Monte Carlo results are in good agreement with the theoretical predictions.

As both Monte Carlo and theoretical results show, the variances are not uniform across the whole FOV. Instead, they are nearly inversely proportional to the f_{jj}'s as shown in (19). If $r_{jj} = 1$ is used, then the variance would be less spatially variant.

IV. Conclusions

We have adapted the theoretical analysis we developed for conventional systems to the new rectangular PEM that has irregular radial and angular sampling. The results allow fast computation of the local impulse response function and covariance. Computer simulation results reveal good agreement between the theoretical approximations and the Monte Carlo results. The theoretical results have also been used to compute SNR for lesion detection. Future work will include modeling randoms and scatters in reconstruction, and validating the results with ROC study and real data from the scanner.

References

[1] P. Virador, W. Moses, and R. Huesman, "Reconstruction in PET cameras with irregular sampling and depth of interaction capability," *IEEE Transactions on Nuclear Science*, vol. 45, pp. 1225–1230, 1998.

[2] W. W. Moses, S. E. Derenzo, C. L. Melcher, and R. A. Manente, "A room temperature LSO/PIN photodiode PET detector module that measures depth of interaction," *IEEE Transactions on Nuclear Science*, vol. 42, pp. 1085–1089, 1995.

[3] R. Huesman, G. Klein, W. Moses, J. Qi, B. Reutter, and P. Virador, "List mode maximum likelihood reconstruction applied to positron emission mammography with irregular sampling," *IEEE Transactions on Medical Imaging*, vol. 19, pp. 532–537, 2000.

[4] J. Qi and R. M. Leahy, "A theoretical study of the contrast recovery and variance of MAP reconstructions from PET data," *IEEE Transactions on Medical Imaging*, vol. 18, pp. 293–305, 1999.

[5] J. Qi and R. M. Leahy, "Resolution and noise properties of MAP reconstruction for fully 3D PET," *IEEE Transactions on Medical Imaging*, vol. 19, pp. 493–506, 2000.

[6] A. Dempster, N. Laird, and D. Rubin, "Maximum likelihood from incomplete data via the EM algorithm," *Journal of Royal Statistical Society, Series B*, vol. 39, pp. 1–38, 1977.

[7] L. Shepp and Y. Vardi, "Maximum likelihood reconstruction for emission tomography," *IEEE Transactions on Medical Imaging*, vol. 1, pp. 113–122, 1982.

[8] K. Lange and R. Carson, "EM reconstruction algorithms for emission and transmission tomography," *Journal of Computer Assisted Tomography*, vol. 8, pp. 306–316, 1984.

[9] J. Qi and R. H. Huesman, "Theoretical study of lesion detectability of MAP reconstruction using computer observers," *IEEE Transactions on Medical Imaging*, vol. 20, 2001, to appear.

[10] H. H. Barrett, J. Yao, J. Rolland, and K. Myers, "Model observers for assessment of image quality," *Proc. Natl. Acad. Sci.*, vol. 90, pp. 9758–9765, 1993.